



# Microstructure and Mechanical Characteristics of AlCoCrFeNi-Based ODS High-Entropy Alloys Consolidated by Vacuum Hot Pressing

K. Raja Rao<sup>1</sup> · Sheetal Kumar Dewangan<sup>2</sup> · A. H. Seikh<sup>3</sup> · Sudip Kumar Sinha<sup>4</sup> · Byungmin Ahn<sup>2,5</sup> 

Received: 27 June 2023 / Accepted: 24 August 2023 / Published online: 13 September 2023  
© The Author(s) under exclusive licence to The Korean Institute of Metals and Materials 2023

## Abstract

The study investigates that a high-entropy alloy based on AlCoCrFeNi is mechanically alloyed (MA) for 40 h with 1 wt% Y<sub>2</sub>O<sub>3</sub> dispersed and then consolidated through vacuum hot pressing (VHP). In VHP, three temperatures are used for consolidation: 800 °C, 900 °C, and 1000 °C. Microanalysis of the powder aggregate formed by MA revealed the presence of mostly face-centered cubic (FCC) and body-centered cubic (BCC) phases, along with a metastable AlFe<sub>4</sub>O<sub>12</sub>Y<sub>3</sub> garnet phase. The enthalpy of mixing Y and Al induced the development of the garnet phase. In addition, after the consolidation of the powder sample at different temperatures, microstructural investigations indicated that the FCC and BCC phases generated during MA were stable owing to sluggish diffusion. By contrast, the garnet phase generated during the MA dissociated into an intermetallic phase based on Yttrium. The slower heating rates associated with VHP (in comparison to the rapid heating rates associated with spark plasma sintering) may be responsible for the dissociation of the garnet phase. The sample sintered at 1000 °C exhibited a bimodal grain distribution, with grain sizes ranging from 100 to 800 nm, as determined by transmission electron microscopy. In addition, this sample had the highest measured hardness of 1353 ± 20 Hv.

**Keywords** High entropy alloy · Mechanical alloying · Vacuum hot pressing · Bimodal grain size · Garnet phase · Intermetallic phase

## 1 Introduction

High-entropy alloys (HEAs) are a unique class of metallic materials that differ from traditional alloys by containing at least five principal elements, leading to significantly higher mixing and configurational entropy in both their solid and liquid states [1–4]. High strength, good ductility, and great wear as well as corrosion resistance are just a few of the remarkable mechanical characteristics that HEAs have to offer [5–10]. Moreover, due to the significant mixing entropy effect, HEAs typically exhibit only one solid solution phase with either a face-centered cubic (FCC) or body-centered cubic (BCC) crystal structure, providing several additional advantages. Owing to these considerations, a considerable number of studies have focused on the development of newer compositions and establishing manufacturing processes to prepare effective HEAs. Even so, the inability of most single-phase HEAs to strike an equilibrium between strength and formability restricts their usefulness [11]. Strength and ductility in single-phase HEAs have proven to be challenging to achieve simultaneously [12]. HEAs with a single-phase FCC structure are ductile, but they are not adequately

✉ K. Raja Rao  
krajarao218@gmail.com

✉ Byungmin Ahn  
byungmin@ajou.ac.kr

<sup>1</sup> Department of Mechanical Engineering, Lendi Institute of Engineering and Technology, Vizianagaram, Andhra Pradesh 535003, India

<sup>2</sup> Department of Materials Science and Engineering, Ajou University, Suwon 16499, Republic of Korea

<sup>3</sup> Mechanical Engineering Department, College of Engineering, King Saud University, 11421 Riyadh, Saudi Arabia

<sup>4</sup> Department of Metallurgical and Materials Engineering, National Institute of Technology Raipur, Raipur, Chhattisgarh 492010, India

<sup>5</sup> Department of Energy Systems Research, Ajou University, Suwon 16499, Republic of Korea

strong. On the contrary, single-phase BCC-structured HEAs potentially offer superior strength at the expense of brittleness [13]. In terms of mechanical properties, it is widely recognized that single-phase high entropy alloys (HEAs) with a body-centered cubic (BCC) structure exhibit low ductility, whereas single-phase HEAs with a face-centered cubic (FCC) structure may demonstrate high ductility but low strength. HEAs with a BCC crystal structure as a single phase have good yield strength at room temperature, but their yield strength decreases significantly as the temperature rises. [7]. In order to achieve an optimal equilibrium between strength and ductility, dual phase high entropy alloys may serve as a viable solution. However, it is worth noting that while these alloys exhibit favorable mechanical properties at room temperatures, their mechanical properties substantially decrease at elevated temperatures. In order to address this issue at higher temperatures, certain modifications can be implemented.

The exceptional creep strength and radiation resistance make nano-structured oxide-dispersion-strengthened (ODS) alloys one of the most promising options for high-temperature applications, including improved fission and fusion reactors [14]. To sustain the yield strength at the elevated temperatures encountered in modern fission and fusion reactors, ODS alloys must be microstructurally stable. Therefore, Ytria ( $Y_2O_3$ ) is added as a dispersoid in ODS alloys because of its excellent thermal stability [15–17]. Similarly, the addition of oxide dispersoids in the HEA system further enhances its microstructural and mechanical properties owing to the pinning action of the dispersoid particles [18].

Gwalani et al. [19] concluded that The  $Al_{0.3}CoCrFeMnNi$  HEA exhibited an increase in compressive yield strength due to the formation of complex oxide particles upon the addition of  $Y_2O_3$ . The compressive yield strength of the HEA was initially measured at 0.98 GPa without  $Y_2O_3$ , but the addition of 3 vol%  $Y_2O_3$  led to an increase to 1.76 GPa. Chen et. al. [20] discovered the effects of dispersed nano-  $Y_2O_3$  (0.5 wt% and 2 wt%) oxide particles on the  $Co_{35}Ni_{30}Fe_{20}Mn_{10}Cr_5$  HEAs subjected to mechanical alloying (MA) and, subsequently, compression under a pressure of 210 kg/cm<sup>2</sup>; finally, the HEAs were sintered at 1150 °C for 60 min. The study results revealed that a surge in milling time contributed to the increase in the size and number of oxide particles. In addition, as the  $Y_2O_3$  content increased, a relative preponderance of nano-oxide particles that spread uniformly throughout the matrix developed. Utilizing MA and spark plasma sintering (SPS) (at 1150 °C), Hadraba et al. [21] developed A  $CoCrFeNiMn$ -based oxide-dispersion-strengthened (ODS) high-entropy alloy (HEA) was synthesized, and At room temperature, it was discovered that this ODS HEA's ultimate strength of tensile and yield strength improved by 30%. At 800 °C, the yield strength increased up to 70% relative to that of  $CoCrFeNiMn$  HEA.

These findings highlight the improvement in the mechanical characteristics of HEAs at high temperatures owing to oxide dispersion strengthening.

In the present study, the  $AlCoCrFeNi$  base HEA system is used, and oxide nanoparticles are uniformly dispersed in the matrix to enhance the overall mechanical properties of the HEA. To better understand the effects of processing temperature on the formation of nanoscale oxides, phase formation, and mechanical properties (specifically, hardness) of the  $AlCoCrFeNi$  HEA with 1 wt%  $Y_2O_3$  addition is studied. The alloyed powders are compacted using the vacuum hot pressing (VHP) technique at sintering temperatures of 800–1000 °C.

## 2 Materials and Methods

Elemental powders of Al, Cr, Co, Fe, and Ni as well as that of  $Y_2O_3$  (Ytria) with purity exceeding 99.4%, were acquired from Sigma Aldrich (India) and used as raw materials in the next synthesis stage. The powders of the individual elements were subjected to MA for 40 h. All elements were mixed in equal proportions (20 at%), and 1 wt% of  $Y_2O_3$  was added during milling in a high-energy ball mill. A tungsten carbide bowl with a capacity of 250 ml and 10-mm balls were used for the purpose. In addition, as a process control agent (PCA) to minimize cold welding during milling, toluene was used. Milling was accomplished with a 10:1 ball-to-powder ratio (BPR), with the vials turning at a constant speed of 250 rpm. To assure alloying during milling, a minimal powder sample was collected for structural characterization after each time interval. The Ytria-dispersed  $AlCoCrFeNi$  alloys were consolidated in a VHP furnace (VB Ceramic Consultants, India). Each MA powder sample was held at the peak temperature for 30 min. The sintering temperatures were set to 800 °C, 900 °C, and 1000 °C, while the heating rate was set to 30 °C/min. Further, the sintering pressure was 35 MPa during the sintering process, and the background vacuum pressure was  $1 \times 10^{-3}$  Pa. Upon removal from the vacuum furnace after cooling, the diameter and thickness of the resulting cylindrical sample were 20 mm and 5 mm, respectively.

An X-ray diffractometer (XRD, PANalytical) equipped with a Cu-K $\alpha$  radiation source ( $\lambda = 0.1540598$  nm) and a scanning electron microscope (SEM, Zeiss EVO-18, Germany) equipped with an energy-dispersive spectrometer (EDS) were used for phase analyses of the milled powders and hot-pressed samples. Furthermore, the microstructures of the sintered samples at the sub-micron scale were examined using transmission electron microscopy (TEM, FEI Technai). The hardness of the sintered samples was investigated using a hardness tester (SHIMADZU) under a load of 9.807 N for 10 s. Particle size was determined using Image J

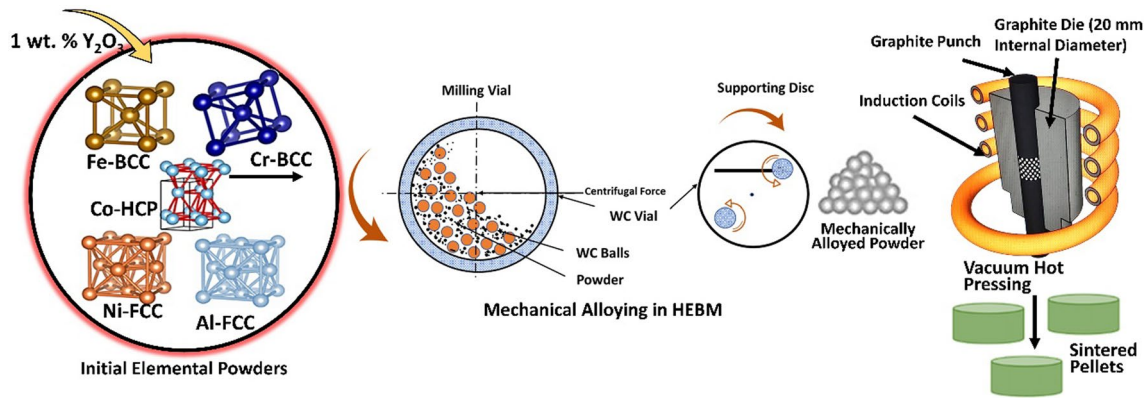


Fig. 1 Schematic representation of the synthesis of AlCoCrFeNi + 1 wt%  $Y_2O_3$  dispersed high-entropy alloy

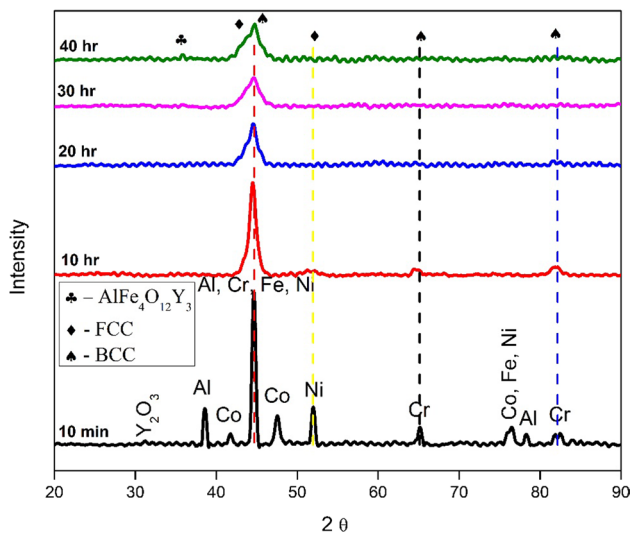


Fig. 2 XRD spectra of nano- $Y_2O_3$ -dispersed AlCoCrFeNi-based HEA at different milling times

(Open-source software for image processing, National Institutes of Health). A schematic illustration of the synthesis process is presented in Fig. 1.

## 3 Results and Discussions

### 3.1 Milled Powder

The X-ray diffraction results obtained for several samples with various milling intervals are depicted in Fig. 2. Upon 10 min of milling, the XRD spectrum exhibited visible reflections for all elements without any indication of alloying. With an increase in ball milling time to 10 h, the intensity and width of the XRD peaks reduced significantly. The decrease in peak intensity indicated the diffusion of elements during the milling process, which results in the development of solid solutions. [22].

The peak reflection of elemental Al dissipated more rapidly because the elements with lower melting temperatures diffused more quickly given that they required lower activation energy for interdiffusion [23]. After 10 h of ball milling, specific peaks related to Al, Co, and  $Y_2O_3$  disappeared, which suggested the likely formation of a solid solution. Following the completion of ball milling, which lasted for 40 h, the FCC and BCC phases were dominant in the matrix. In addition to these two phases, another unnamed garnet phase with a cubic crystal structure was observed. Moreover,  $AlFe_4O_{12}Y_3$  was developing at the end of 40 h of milling. The corresponding JCPDS file for this phase is 98–009–3627, with  $Ia\bar{3}d$  as the space group.

The enthalpy of mixing between the elements Y and Al, whose value is  $-38.00$  kJ/mol, may have led to the

**Table 1** EDS quantification of points (at%) for the HP AlCoCrFeNi ODS-HEA sintered at  $1000^\circ C$

EDS regions	Elemental composition (at%)						
	Al	Co	Cr	Fe	Ni	Y	O
A	52.47	3.87	26.23	6.16	7.32	1.79	2.16
B	21.87	23.57	20.01	10.12	18.34	0.05	6.04
C	13.68	1.23	54.01	11.49	1.98	0.05	17.56

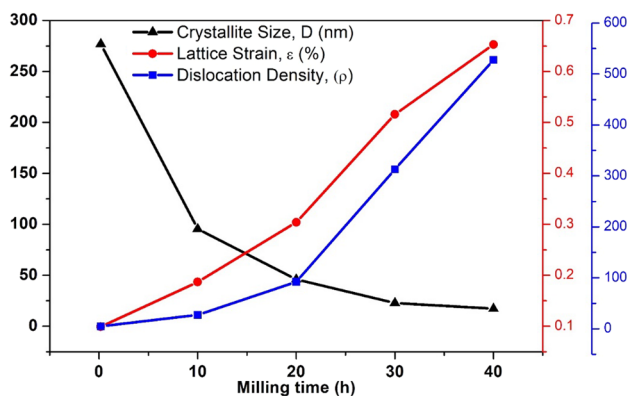


**Fig. 3** Estimated values of crystallite size (D), lattice strain ( $\epsilon$ ), and dislocation density ( $\rho$ ) of different alloy systems subjected to different milling times

formation of this garnet phase. Among Yttrium and all the other elements in the system, this negative enthalpy magnitude is the most significant in this system [24]. A similar complex-phase development was observed in a previous study [25]. The unit cell lattice parameters of the garnet phase were determined to be  $a = 12.2620 \pm 0.008 \text{ \AA}$ . The interplanar distances for the (111), (200), and (220) planes of the FCC phase were measured as 2.03, 1.76, and 1.24, respectively. The interplanar distances for the (110), (200), and (211) planes of the BCC phase were measured as 2.05  $\text{\AA}$ , 1.44  $\text{\AA}$ , and 1.18  $\text{\AA}$ , respectively. The calculated lattice parameters of the FCC and BCC unit cells were found to be  $3.5060 \pm 0.03$  and  $2.8780 \pm 0.04 \text{ \AA}$ , respectively, which are consistent with previously reported values for the AlCo-CrFeNi HEA. [7]. Table 1 summarizes the results calculated using the Scherrer (Eq. 1) and Williamson–Hall equations (Eq. 2) for the most intense peak in the spectrum [26]. Moreover, we used Eq. 3 to determine dislocation density as a function of milling time [27].

$$D = 0.94\lambda / \beta \cos \theta \quad (1)$$

$$\beta \cos \theta = \frac{0.94\lambda}{D} + 4 \epsilon \sin \theta \quad (2)$$

$$\rho = 2\sqrt{3} \frac{(\epsilon)}{D \times b} \quad (3)$$

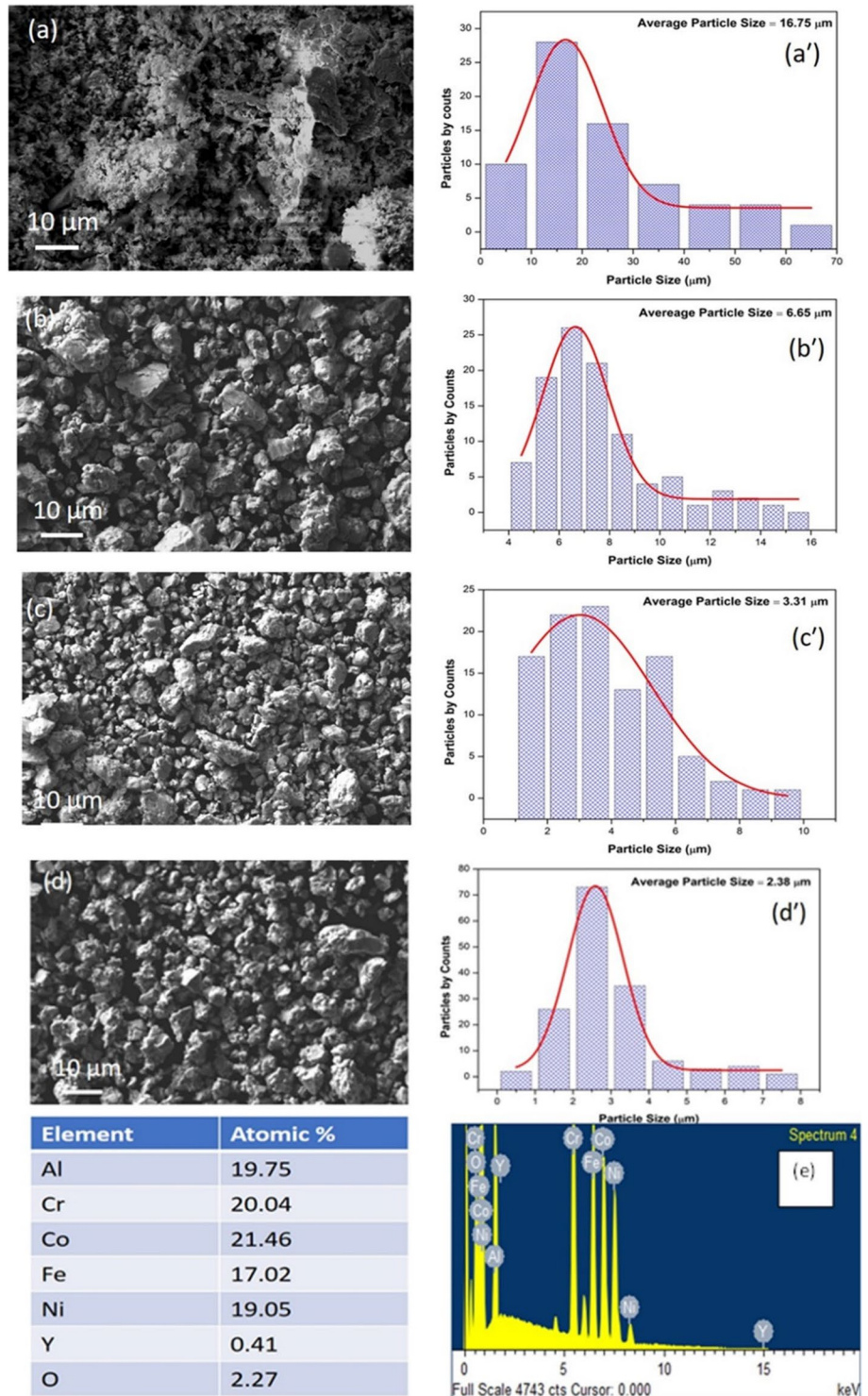
where the dislocation density ( $\rho$ ), Burgers vector ( $b$ ), the crystallite size ( $D$ ), lattice strain ( $\epsilon$ ), and full width at half maxima ( $\beta$ ) have been presented in which the Bragg peaks (in radian), Bragg angle (in  $\theta$ ) while the wavelength presents as ( $\lambda$ ) for the analyzed peak of the X-ray.

The results depicted in Fig. 3 demonstrate that the average crystallite size experiences a sharp decline from 276.9 nm to a minimum of 95.4 nm when the ball milling time increases

from 10 min (0 h) to 10 h. With further milling, the crystallite size decreases gradually, reaching a steady-state value of 17.2 nm at 40 h of milling. Prolonged milling leads to an increase in both the lattice strain and dislocation density, which exhibit significant fluctuations throughout the process. The lattice strain ranges from 0.099 to 0.653%, while the dislocation density ranges from  $4.91 \times 10^{15}$  to  $527.60 \times 10^{15} / \text{m}^2$ . The presence of hard elements ( $\text{Y}_2\text{O}_3$  particles) in the alloy system induces brittleness and eases the breaking of alloy particles. In addition, it causes the dislocation density to increase to a much higher extent as the milling time increases. Thus, these stages are reached because of the milling process [28]. During ball milling, the addition of 1 wt%  $\text{Y}_2\text{O}_3$  does not substantially affect the primary phases that are developed [29]. SEM micrographs show the morphology and distribution of the as-milled alloy powder aggregates. After 10 min of milling, the particle morphology is asymmetrical, and the particle size is hefty, as shown in the SEM micrographs in Fig. 4a–d. Figure 4a'–d' show histograms of the particle size distributions corresponding to these SEM micrographs. In addition, When  $\text{Y}_2\text{O}_3$  particles with high entropy alloy powder are milled, their morphology changes to a plate-like morphology. As deformation increases, work hardening and brittleness occur, and these plate-like particles break into smaller particles. Thus, the decrease in particle size resulting from work hardening can be attributed to the inclusion of hard and brittle  $\text{Y}_2\text{O}_3$  particles. Therefore, the reduction in particle size observed during the milling process is attributed to the work-hardening effect, resulting in a decrease in particle size after 10 h of milling. This trend is evident in the XRD patterns, where an increase in lattice strain leads to a decrease in crystallite size. The trend in particle size observed in Fig. 4a'–d' is consistent with the XRD study, where increasing the milling duration in the MA process from 10 min to 40 h resulted in a decrease in particle size from 16.75 to 2.38  $\mu\text{m}$ , respectively. After milling for a total of 40 h, the estimated particle size was 2.38  $\mu\text{m}$ . The EDS spectrum shown in Fig. 4e depicts the elemental composition of the powders that were ball-milled for 40 h. The homogeneity of the elements appeared to be visible from this result because the atomic percentages of all the key elements were close to 19%. All the elements are present in the system, as indicated by the EDS mapping. In addition, the EDS maps obtained before and after milling of the HEA powder are presented in Fig. 5a and b, respectively. According to these EDS maps, the homogeneous distribution of the elements is contemporary in the HEAs, which led to the production of solid solutions after the completion of the MA process.



**Fig. 4** SEM images of nano- $Y_2O_3$ -dispersed AlCoCr-FeNi-based HEAs at different milling times with the corresponding particle size distribution histograms: (a, a'), (b, b'), (c, c'), and (d, d') 10 min, 10 h, 20 h, 30 h, and 40 h respectively. (e) Distribution of elements in EDS spectra



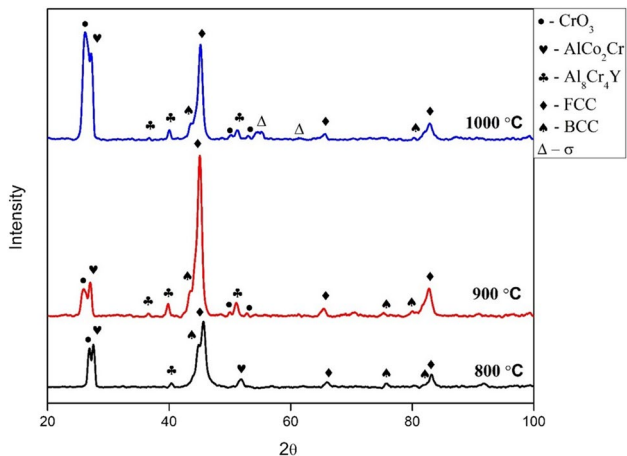
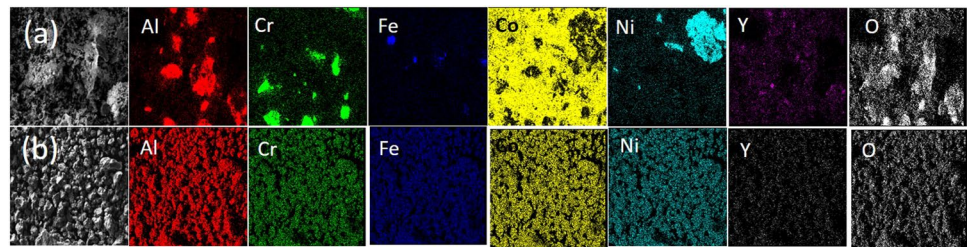
### 3.2 Vacuum Hot-Pressed Samples

Figure 6 presents the X-ray diffraction patterns of the HEAs obtained after VHP at different sintering temperatures. Following the completion of the alloying process, the XRD pattern of the AlCoCrFeNi-based ODS-HEA powder revealed

the development of an FCC and BCC phase matrix, in addition to the existence of a small garnet phase ( $AlFe_4O_{12}Y_3$ ), as described in the preceding section.

The garnet phase formed during MA dissociated during sintering into a Yttrium-based intermetallic structure ( $Al_3Cr_4Y$ , JCPD # 98–005-7664) and chromium oxide

**Fig. 5** EDS elemental mapping of HEAs **a** before and **b** after milling



**Fig. 6** XRD spectra of nano- $Y_2O_3$ -dispersed AlCoCrFeNi-based HEAs at different temperatures

( $CrO_3$ ). Because it accounted for only 1% of the overall weight of the HEA system, the tiny Yttrium-based intermetallic phase exhibited an extremely low intensity. In the study of nano- $Y_2O_3$ -dispersed ferritic steel through MA with hot isostatic pressing, comparable observations of the Yttria-based intermetallic phases were recorded [29]. Additionally, a stable phase (that is Cr-rich) exists at 1000 °C. A comparison between the noticeable XRD peaks of the VHP samples and the MA powder peaks of the equivalent compositions revealed an average decrease in peak width (FWHM), as illustrated in Fig. 2. During the sintering procedure, lattice strain was relieved, which reduced the FWHM. The lattice strain was released during sintering, which in turn, reduced the FWHM. The FCC phase mainly contained Al, Ni, and Co, while the BCC phase mainly contained elemental Al, Cr, and Fe. However, notably, for the sample sintered at 800 °C, the peaks based on Yttria are nominal. From the peak locations of the intermetallic Yttria-based phase, there is only a marginal difference in this phase at higher temperatures. Zeybek et al. [30] demonstrated how the mechanical characteristics of AISI 410 L steel are influenced by the particle size of Yttria (900 nm and 50 nm) and how the formations of  $Y_2Si_2O_7$  and other inclusions proceed in the normal and heat-treated states. The experimental results indicate that larger, more complex oxide particles ( $Y_2Si_2O_7$ ) dissolved/

dissociated before the smaller ones under heat treatment. The sizes of both the complex oxide and pure Yttria particles changed significantly and simultaneously. Alongside the FCC and BCC phases, another intermetallic phase called “ $AlCo_2Cr$ ” was formed at the  $2\theta$  Bragg angles of  $26.789^\circ$  and  $52.987^\circ$ , and its peak intensity increased as the sintering temperature increased. The reason underlying the increase in the  $AlCo_2Cr$  phase in the XRD spectrum at higher sintering temperatures can be attributed to higher temperatures during sintering, MA of powders to ensure that their conditions shift from metastable to stable. The phenomenon could be brought on by the substantial surplus energy associated with elevated dislocation densities and the abundance of nano-crystalline barriers in the MA powders, both of which considerably reduced the activation energy needed for phase transition [31]. In addition, Cr–Fe/Cr–Co/Cr–Fe–Co intermetallic compounds were responsible for the observed sigma phases rich in Cr (1000 °C) [21].

Figure 7a–c shows the SEM micrographs of the ODS-HEA samples at several sintering temperatures and Fig. 7d–f shows the corresponding high-resolution versions of the images in Fig. 7a–c. Figure 7a shows the SEM micrograph of the ODS-HEA sintered at 800 °C. The micrograph shows two different regions containing bright grey grains and dark grain boundaries, separately. In Fig. 7a, the bright grey region is consistent with the FCC phase, which is rich in Ni, Fe, and Co, whereas the dark grain boundaries are rich in Cr and Fe, and they correspond to the BCC crystal structure. Moreover, SEM images complement XRD findings that show the FCC to be the dominant phase in all the sintered samples. Phase fractions evaluated from SEM images are 800 °C—FCC/BCC (73%:27%), 900 °C—FCC/BCC (66%:34%), and 1000 °C—FCC/BCC (61%:39%). Figure 7d shows high-magnification versions of the images in Fig. 7a. Point A represents an area that is rich in Al, Cr, and Y, and it is built through the progression of sintering due to the dissolution of the garnet phase. The EDS analysis data corresponding to points A, B, and C are presented in Table 1. In addition, Fig. 7b and c present results that are comparable to those revealed in Fig. 7a, although the grey regions in Fig. 7b and c exhibit more limited differences in terms of colour contrast. We believe that the FCC and BCC phases include elements with atomic numbers that are too close to each other [23]. Additionally, in Fig. 7f, point C



**Fig. 7** Lower-magnification SEM images of ODS-HEA prepared using HP at **a** 800 °C, **b** 900 °C, and **c** 1000 °C; **d**, **e**, and **f** are the corresponding higher-magnification images

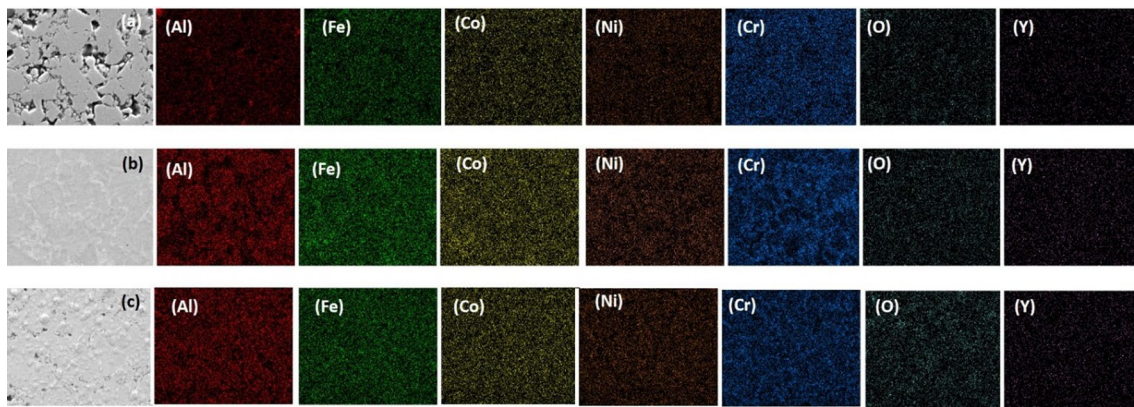
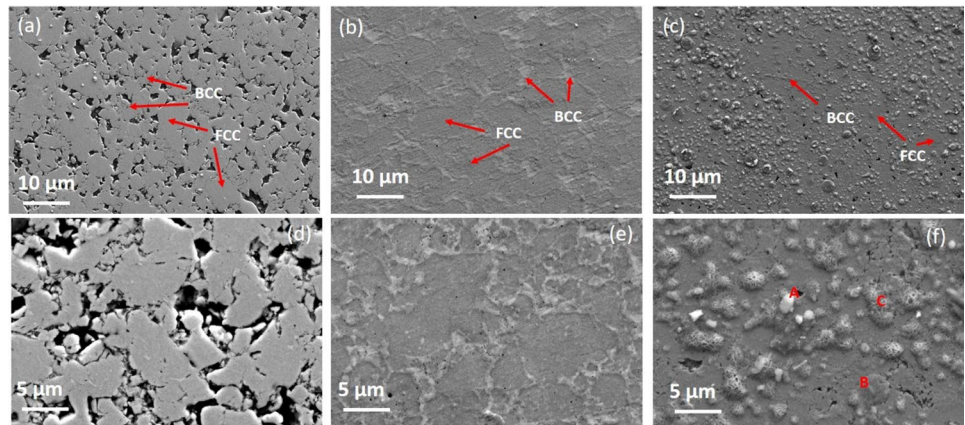


**Fig. 8** Elemental distribution of AlCoCrFeNi ODS-HEA prepared using HP at several temperatures: **a** 800 °C, **b** 900 °C, and **c** 1000 °C

denotes chromium oxide, which is clearly visible. This oxide might have formed owing to the higher sintering temperature and the longer holding time at this temperature. The elemental maps of each of the elements in the Ytria-mixed alloys are shown in Fig. 8. At 900 °C and 1000 °C, we discovered Cr dispersion in the HP sample. The Yttrium-based phase, however, was distributed consistently throughout the entire microstructure of the HP samples sintered at three distinct temperatures, which indicated the stability of this phase. The Yttrium-based phase appears at low levels in the compositions, and as a consequence, the mapping photos show that the chemical element "Y" appears in extremely small amounts. The quantity of Ytria ( $Y_2O_3$ ) utilized in the samples was 1 wt% of the entire amount of HEA.

The results of a TEM examination of the AlCoCrFeNi ODS-HEA sintered at 1000 °C are depicted in Fig. 9. Figure 9a shows a bright-field TEM image, and according to this image, the grains have a bimodal distribution. As shown by the histogram in Fig. 9c, the grain size can range between 100 and 800 nm. This bimodal grain formation could have occurred as a result of the combination of the solid solution and the intermetallic phase at 1000 °C, as seen in the

XRD analysis findings. It was found that the AlCoCrFeNi ODS-HEA sintered at 1000 °C had an average grain size of  $194 \pm 23$  nm. The interplanar spacing of the distributed nanoparticles (intermetallic phase) is shown in the HRTEM lattice fringe image, and the measured  $d$ -spacing value is 0.242 nm. From the XRD analysis, it was determined that the complex yttrium-based garnet phase had a  $d$ -spacing value of 0.224 nm. This  $d$ -spacing value is almost equal to the measured value. This confirmed the development of the Yttrium-based intermetallic phase.

### 3.3 Mechanical Characteristics of VHP Samples

The estimated room-temperature hardness values of the VHP ODS-HEA alloys sintered at 800 °C, 900 °C, and 1000 °C are depicted in Fig. 10.

The experimental investigation indicated that the hardness values of the AlCoCrFeNi ODS-HEAs formed by VHP and sintered at 800 °C, 900 °C, and 1000 °C were  $858 \pm 15$  HV,  $944 \pm 10$  HV, and  $1353 \pm 20$  HV, respectively. An earlier study on AlCoCrFeNi HEA synthesized through MA and SPS yielded a hardness value of 815 HV (8 GPa)

**Fig. 9** **a** TEM bright-field image of AlCoCrFeNi ODS-HEA. **b** HRTEM image of AlCoCrFeNi ODS-HEA sintered at 1000 °C. **c** Histogram of grain size distribution corresponding to **a**

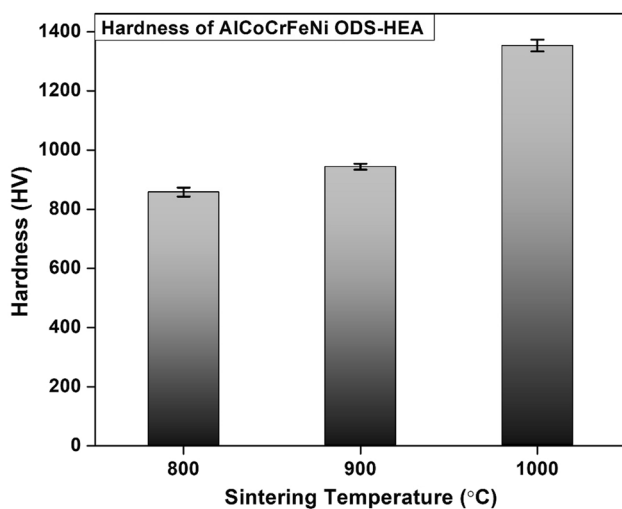
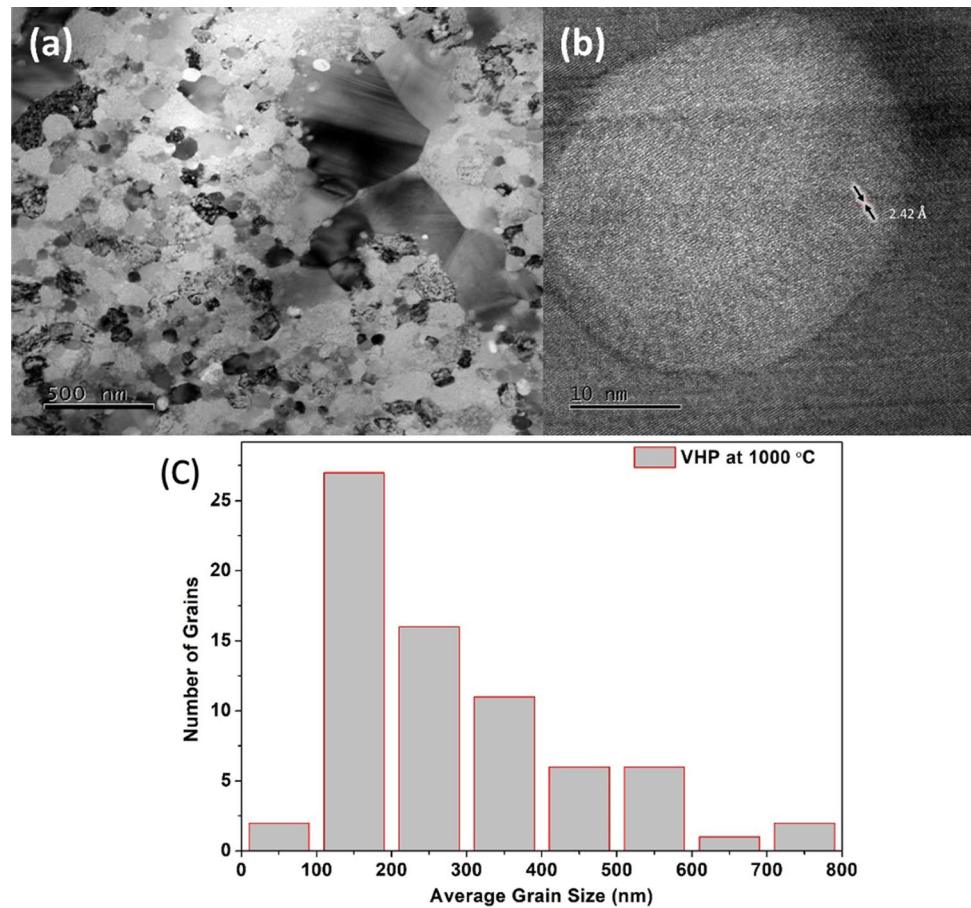


**Fig. 10** Sintering temperature and Vickers hardness of ODS-HEAs

for the base AlCoCrFeNi HEA (Sintered at 1000 °C) [32]. A hardness test was used to determine the hardness of the ODS-HEA sample sintered at 1000 °C, and the resulting hardness value was approximately 52% higher than that of the base AlCoCrFeNi HEA. The variation of hardness

with sintering temperature was linear. Furthermore, the findings of the XRD and SEM examinations supported the hypothesis that the chromium oxide and phases existing in the alloy sintered at 1000 °C were responsible for the rise in hardness value from 944 to 1353 HV.

## 4 Conclusions

A HEA based on AlCoCrFeNi with dispersed  $Y_2O_3$  (1 wt%) was synthesized from elemental powders by a combination of ball milling and VHP. In addition to the formation of a hard insoluble garnet phase,  $AlFe_4O_{12}Y_3$  with a cubic crystal structure and lattice parameters of  $a = 12.2620 \pm 0.008 \text{ \AA}$  was formed. These alloys exhibited a dual phase after 40 h of milling. The lattice values of the FCC and BCC phases were 3.5060 Å and 2.8780 Å, respectively. Ball milling for 10 min to 40 h caused a variation in the lattice strain from 0.099 to 0.653%. After 40 h of ball milling, the dislocation density was significantly higher than before owing to the incorporation of nanoscale  $Y_2O_3$  particles.



After the consolidation of the MA powder by VHP, the FCC and BCC phases were retained, but the garnet phase transformed into a Yttrium-based intermetallic structure of  $\text{Al}_8\text{Cr}_4\text{Y}$  and chromium oxide ( $\text{CrO}_3$ ). The TEM results revealed that the sample sintered at 1000 °C exhibited a bimodal grain distribution with an average grain size of  $194 \pm 23$  nm. The temperature at which the ODS-HEAs were processed during VHP critically influenced the mechanical characteristics of the resulting materials. When the VHP temperature was increased from 800 to 1000 °C, the hardness values increased. In this study, the maximum attained hardness value was 1353 HV at the sintering temperature of 1000 °C.

**Acknowledgements** The authors would like to acknowledge the Researchers Supporting Project number (RSP2023R373), King Saud University, Riyadh, Saudi Arabia.

**Funding** This research was funded by the Researchers Supporting Project number RSP2023R373.

## Declarations

**Conflict of interest** The author declares no competing financial interests. One of the coauthors, Byungmin Ahn, is a current editor of the Metals and Materials International journal.

## References

- B.S. Murty, J.W. Yeh, S. Ranganathan, in *High Entropy Alloys* (Butterworth-Heinemann, Oxford, 2014), pp. 13–35, <https://doi.org/10.1016/B978-0-12-800251-3.00002-X>
- C. Nagarjuna, S.K. Dewangan, A. Sharma, K. Lee, S.J. Hong, B. Ahn, *Met. Mater. Int.* **29**, 1968 (2023). <https://doi.org/10.1007/S12540-022-01355-W>
- A. Sharma, H. Lee, B. Ahn, *Met. Mater. Int.* **28**, 2216 (2022). <https://doi.org/10.1007/S12540-021-01125-0>
- J.W. Yeh, S.K. Chen, S.J. Lin, J.Y. Gan, T.S. Chin, T.T. Shun, C.H. Tsau, S.Y. Chang, *Adv. Eng. Mater.* **6**, 299 (2004). <https://doi.org/10.1002/ADEM.200300567>
- M.H. Tsai, J.W. Yeh, *Mater. Res. Lett.* **2**, 107 (2014). <https://doi.org/10.1080/21663831.2014.912690>
- K.R. Rao, S.K. Sinha, *Vacuum* **184**, 109802 (2021). <https://doi.org/10.1016/j.vacuum.2020.109802>
- K.R. Rao, S.K. Sinha, *Mater. Sci. Eng. B* **281**, 115720 (2022). <https://doi.org/10.1016/j.mseb.2022.115720>
- K.R. Rao, S.K. Sinha, *Manuf. Lett.* **20**, 5 (2019). <https://doi.org/10.1016/j.mfglet.2019.02.004>
- S.K. Dewangan, D. Kumar, S. Samal, V. Kumar, *J. Mater. Eng. Perform.* **30**, 4421 (2021). <https://doi.org/10.1007/s11665-021-05552-3>
- S. K. Dewangan, Studies on Microstructure, Mechanical and High-Temperature Oxidation Behaviour of Tungsten Containing High Entropy Alloys, (Indian Institute of Technology Indore, 2021), <http://dspace.iiti.ac.in:8080/jspui/handle/123456789/307>. Accessed 1 Sep 2021
- Z. Liang, Y. Zhang, Y. Liu, Z. Zhu, H. Zhang, *Mater. Lett.* **317**, 132092 (2022). <https://doi.org/10.1016/j.matlet.2022.132092>
- Y. Zhang, T.T. Zuo, Z. Tang, M.C. Gao, K.A. Dahmen, P.K. Liaw, Z.P. Lu, *Prog. Mater. Sci.* **61**, 1 (2014). <https://doi.org/10.1016/j.pmatsci.2013.10.001>
- O.N. Senkov, G.B. Wilks, J.M. Scott, D.B. Miracle, *Intermetallics* **19**, 698 (2011). <https://doi.org/10.1016/j.intermet.2011.01.004>
- B. Raj, U.K. Mudali, *Proc. Indian Natl. Sci. Acad.* **81**, 801 (2015). <https://doi.org/10.16943/ptinsa/2015/v81i4/48298>
- S.S. Kumar, S. ES, S.B. Chandrasekhar, S.K. Karak, *Mater. Res.* **19**, 175 (2016). <https://doi.org/10.1590/1980-5373-MR-2015-0593>
- J.M. Byun, C.W. Park, Y.D. Kim, *Met. Mater. Int.* **24**, 1309 (2018). <https://doi.org/10.1007/S12540-018-0136-1>
- C. Suryanarayana, A.A. Al-Joubori, Z. Wang, *Met. Mater. Int.* **28**, 41 (2022). <https://doi.org/10.1007/S12540-021-00998-5>
- S. Ohtsuka, S. Ukai, M. Fujiwara, T. Kaito, T. Narita, *Mater. Trans.* **46**, 3 (2005). <https://doi.org/10.2320/matertrans.46.487>
- B. Gwalani, R.M. Pohan, O. Ahmed, T. Alam, S. Hyung, H. Jin, R. Banerjee, *Scr. Mater.* **162**, 477 (2019). <https://doi.org/10.1016/j.scriptamat.2018.12.021>
- C.L. Chen, *Intermetallics* **113**, 106570 (2019). <https://doi.org/10.1016/j.intermet.2019.106570>
- H. Hadraba, Z. Chlup, A. Dlouhy, F. Dobes, P. Roupčová, M. Vilemova, J. Matejíček, *Mater. Sci. Eng. A* **689**, 252 (2017). <https://doi.org/10.1016/j.msea.2017.02.068>
- S. Varalakshmi, M. Kamaraj, B.S. Murty, *J. Alloys Compd.* **460**, 253 (2008). <https://doi.org/10.1016/j.jallcom.2007.05.104>
- A. Dwivedi, C.C. Koch, K.V. Rajulapati, *Mater. Lett.* **183**, 44 (2016). <https://doi.org/10.1016/j.matlet.2016.07.083>
- A. Takeuchi, A. Inoue, *Mater. Trans.* **46**, 2817 (2005). <https://doi.org/10.2320/matertrans.46.2817>
- B. Gwalani, R.M. Pohan, J. Lee, B. Lee, R. Banerjee, H.J. Ryu, S.H. Hong, *Sci. Rep.* **8**, 14085 (2018). <https://doi.org/10.1038/s41598-018-32552-6>
- M. Murali, S.P.K. Babu, B.J. Krishna, A. Vallimananalan, *Prog. Nat. Sci.: Mater. Int.* **26**, 380 (2016). <https://doi.org/10.1016/j.pnsc.2016.06.008>
- K.R. Rao, S.K. Sinha, *Mater. Sci. Forum* **978**, 145 (2020). <https://doi.org/10.4028/www.scientific.net/MSF.978.145>
- A. Patra, R. Saxena, S.K. Karak, T. Laha, S.K. Sahoo, *J. Alloys Compd.* **707**, 245 (2017). <https://doi.org/10.1016/j.jallcom.2016.11.424>
- S.K. Karak, T. Chudoba, Z. Witczak, W. Lojkowski, I. Manna, *Mater. Sci. Eng. A* **528**, 7475 (2011). <https://doi.org/10.1016/j.msea.2011.06.039>
- A. Zeybek, S. Pirfo Barroso, K.B. Chong, L. Edwards, M.E. Fitzpatrick, *J. Mater. Eng. Perform.* **23**, 2120–2130 (2014). <https://doi.org/10.1007/s11665-014-0988-6>
- H. Cheng, W. Chen, X. Liu, Q. Tang, Y. Xie, P. Dai, *Mater. Sci. Eng. A* **719**, 192 (2018). <https://doi.org/10.1016/j.msea.2018.02.040>
- S. Mohanty, T.N. Maity, S. Mukhopadhyay, S. Sarkar, N.P. Gurao, S. Bhowmick, K. Biswas, *Mater. Sci. Eng. A* **679**, 299 (2017). <https://doi.org/10.1016/j.msea.2016.09.062>

**Publisher's Note** Springer Nature remains neutral with regard to jurisdictional claims in published maps and institutional affiliations.

Springer Nature or its licensor (e.g. a society or other partner) holds exclusive rights to this article under a publishing agreement with the author(s) or other rightsholder(s); author self-archiving of the accepted manuscript version of this article is solely governed by the terms of such publishing agreement and applicable law.